



# Unbalanced discharging and aging due to temperature differences among the cells in a lithium-ion battery pack with parallel combination



Naixing Yang, Xiongwen Zhang<sup>\*</sup>, BinBin Shang, Guojun Li

Key Laboratory of Thermal-Fluid Science and Engineering of MOE, School of Energy & Power Engineering, Xi'an Jiaotong University, 710049, China

## HIGHLIGHTS

- A thermal–electrochemical model is developed for the parallel-connected cells.
- Temperature differences among the cells cause unbalanced discharging and aging.
- A greater temperature difference results in a larger capacity loss of the pack.

## ARTICLE INFO

### Article history:

Received 18 August 2015  
Received in revised form  
18 November 2015  
Accepted 17 December 2015  
Available online 28 December 2015

### Keywords:

Lithium-ion batteries  
Parallel-connected cells  
Temperature difference  
Discharge  
Capacity loss

## ABSTRACT

This paper presents an investigation on the unbalanced discharging and aging due to temperature difference between the parallel-connected cells. A thermal–electrochemical model is developed for the parallel-connected battery pack. The effects of temperature difference on the unbalanced discharging performances are studied by simulations and experiments. For the parallel-connected cells, the cell at higher temperature experiences a larger current in the early discharging process before approximately 75% of depth of discharge (DOD). When the discharge process approaches the voltage turn point of the battery pack, the discharge current through the cell at higher temperature begins to decrease significantly. After the DOD reaches approximately 90%, the discharge current of the cell at higher temperature rises again. Correspondingly, the changes in the discharging current through the cell at lower temperature are opposite to that of the cell at higher temperature. Simulations also show that the temperature difference between the parallel-connected cells greatly aggravates the imbalance discharge phenomenon between the cells, which accelerates the losses of the battery pack capacity. For the parallel-connected battery pack, the capacity loss rate approximately increases linearly as the temperature difference between the cells increases. This trend is magnified with the increase of operating temperature.

© 2015 Elsevier B.V. All rights reserved.

## 1. Introduction

Lithium-ion batteries show a great potential for powering electric vehicles (EVs) and hybrid electric vehicles (HEVs) due to their superior energy density, high specific energy and no memory effect etc. [1]. It is widely known that the operating temperature gives significant effects on the charging/discharging performances (e.g., voltage platform, discharge capacity and service life, etc.) of the lithium-ion batteries [2–5]. A lower operating temperature (<20 °C) leads to the reductions of the battery power capability and

driving range, and even the freezing phenomenon with electrolyte. On the other hand, the battery capacity degradation is aggravated when operating at extreme high temperatures (>45 °C), which may induce occurrence of the battery thermal runaway. Therefore, a thermal management system is essential for maintaining the temperature of the cells in the battery pack at desired levels. Usually, the optimal operating temperature for the lithium-ion batteries is in the range of 20 °C–45 °C, which enables to maximize the battery power (or capacity) capability and lifetime.

A few types of battery thermal management system (BTMS) have been reported in Refs. [6–14], primarily including the air-based thermal management system [6–10], the liquid-based thermal management system [11,12], and the phase change material (PCM) thermal management system [13,14] etc. Because of the

<sup>\*</sup> Corresponding author.

E-mail address: [xwenz@mail.xjtu.edu.cn](mailto:xwenz@mail.xjtu.edu.cn) (X. Zhang).

advantages of ease of operation, low production costs and little space occupation, the air-based thermal management system has been widely applied in the EVs or HEVs [14]. In the air-based cooling systems, the air is channeled from the heat exchanger into a series of ducts or channels that drive the air through the cells or modules forcing the heated air out of the battery pack and back into the heat exchange system. When the EVs drive at higher ambient temperature ( $>35^\circ\text{C}$ ) or consume larger power (accelerating or climbing), the air-based cooling system is required to lower the inlet air temperature or increase the cooling air flux to avoid the battery overheat. This increases the temperature differences within the battery pack, leading to unbalanced discharging phenomenon among the cells. In addition, the cells far from the cooling air inlet have relatively higher temperature that results in greater capacity degradation rate [15–17], which induces the unbalanced aging phenomenon among cells in the battery pack. This divergence of cells greatly shortens the total deliverable capacity and the service life of the battery pack. An important target for BTMS design is to minimize the temperature differences among the cells in the pack.

A battery pack for EVs or HEVs is formed by a multitude of cells connected in series or/and parallel to deliver the desired driving power and capacity. The uneven temperature distribution within the pack leads to mismatch of the internal resistance among cells. For a battery pack with series combination, all the cells have the same charging/discharging current. The cutoff voltage is determined by the weakest cell among the serial-connected cells, which thus affects the overall capacity of the battery pack [18]. Unlike the series-connected cells, the current differences among the cells with parallel combination are caused by the mismatch of the cell internal resistance. The unmatched internal resistance among the parallel-connected cells causes unbalanced discharging and ageing performances. Generally, the current in each parallel-cell branch is not all monitored in the EV battery management systems. Pre-assessments of unbalanced discharging and ageing performances due to temperature differences among the cells are essential in the battery assembly and design of thermal management systems.

The discharging performances for different cell assembly configurations were studied by researchers [19,20]. Wu et al. [19] proposed a semi-experimental method for calculating the discharging voltage and capacity of cells in series and/or parallel-connected battery pack. However, the effects of the temperature difference within battery pack on the cell unbalanced discharging were not considered in their work. R. Gogoana et al. [20] experimentally investigated the effects of the internal resistance mismatch of cells on the discharging performances for a parallel-connected battery pack. This work is devoted to study the effects of temperature difference on the unbalanced discharging and ageing performances in the parallel-connected cells. A thermal–electrochemical model is developed and is used to simulate the discharging process of the battery pack with parallel combination. The influences of the temperature differences between the parallel-connected cells on the discharging performances are analyzed in detail. An experiment-based simplified capacity degradation model is developed for the lithium-ion battery. The dependence between the cell temperature difference and the capacity loss rate is quantified for the battery pack with parallel combination.

## 2. Model development

The electrochemical-thermal model of lithium-ion batteries is developed on the basis of the mass conversion equations, the charge conversion equations [21–23] and the energy balance equation [23,24]. A schematic diagram of the battery electrochemical-thermal model is illustrated in Fig. 1, which includes a pseudo 2D electro-chemical model in the electrode

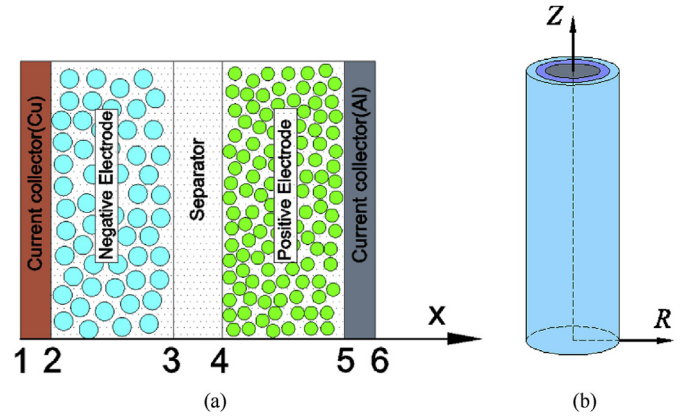


Fig. 1. Schematics of the lithium-ion battery thermal–electrochemical model: (a) Electrochemical model and (b) Thermal model.

thickness scale (see Fig. 1(a)) and a 2D thermal model in the single battery scale (see Fig. 1(b)). The main components of a unit cell consist of a negative electrode, a separator, a positive electrode, bound by two current collectors. The basic assumptions of the proposed model are listed as follows:

- (a) Active materials in two electrodes are considered to be composed of spherical particles with uniform size.
- (b) The electrolyte is assumed to be binary with only  $\text{Li}^+$  as the electroactive species.
- (c) Electrochemical performance along the spiral direction is assumed to be homogenous.
- (d) Side reaction during discharging/charging process is neglected.

Based on the above assumptions, the battery energy equation is calculated in a 2D axis-symmetric model [23].

### 2.1. Governing equations

#### 2.1.1. Mass conversion equations

According to the Fick's 2nd law, the mass conservation of Li in the active particles of both electrodes is expressed by

$$\frac{\partial c_{s,i}}{\partial t} = \frac{D_{s,i}}{r^2} \frac{\partial}{\partial r} \left( r^2 \frac{\partial c_{s,i}}{\partial r} \right) \quad (1)$$

where  $i = n$  and  $p$ . The boundary conditions are described by

$$-D_{s,i} \frac{\partial c_{s,i}}{\partial r} \bigg|_{r=0} = 0 \quad (2)$$

$$-D_{s,i} \frac{\partial c_{s,i}}{\partial r} \bigg|_{r=r_{s,i}} = j_i \quad (3)$$

According to the concentrated solution theory, the mass conservation of  $\text{Li}^+$  in the electrolyte is given by

$$\epsilon_{l,i} \frac{\partial c_l}{\partial t} = D_{\text{eff},i} \frac{\partial^2 c_l}{\partial x^2} + a_i (1 - t_+) j_i \quad (4)$$

where  $i = n, s$  and  $p$ . The effective diffusion coefficient of Li in the electrolyte,  $D_{\text{eff},i}$  is given by  $D_{\text{eff},i} = D_{\text{eff},i}^{\text{true}}$ , which takes into account the effect of tortuosity on  $\text{Li}^+$  transportation. The specific surface area of electrode particles is calculated by  $a_i = 3\epsilon_{s,i}/r_{s,i}$ . The boundary conditions are given by

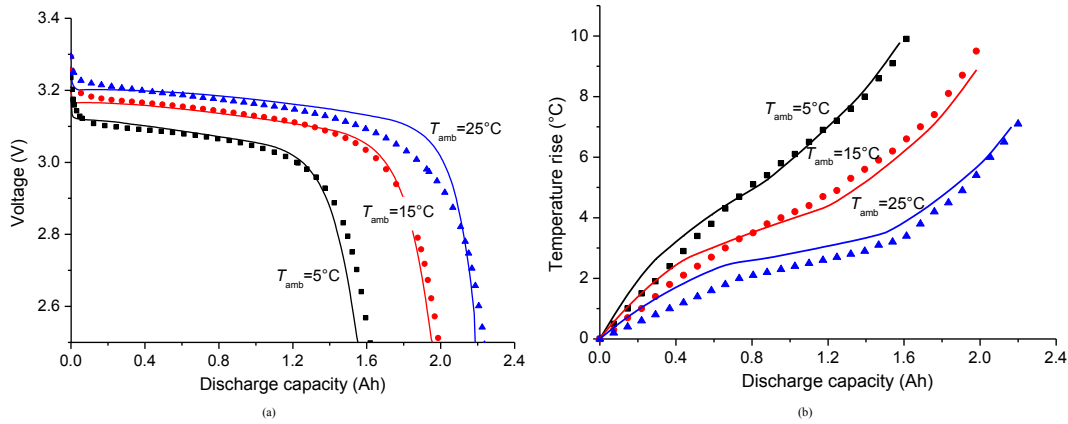


Fig. 2. Comparison between the experimental (dots) and numerical results (solid lines) during discharge at different ambient temperatures: (a) Voltage and; (b) Temperature.

$$D_{eff,i} \frac{\partial c_i}{\partial x} \Big|_{x=2} = D_{eff,i} \frac{\partial c_i}{\partial x} \Big|_{x=5} = 0 \quad (5)$$

where 2 and 5 are the boundary points in the direction of cell thickness (see Fig. 1).

### 2.1.2. Charge conversion equations

The charge conversion equation in the solid electrode material is governed by Ohm's law:

$$i_{s,i} = -\sigma_{eff,i} \frac{\partial \phi_{s,i}}{\partial x} \quad (6)$$

where  $i = n$  and  $p$ . The effective electric conduction is given by  $\sigma_{eff,i} = \sigma_i \epsilon_s$ . The boundary conditions are given by

$$\phi_s|_{x=1} = 0 \quad (7)$$

$$-\sigma_{eff,i} \frac{\partial \phi_{s,i}}{\partial x} \Big|_{x=3} = -\sigma_{eff,i} \frac{\partial \phi_{s,i}}{\partial x} \Big|_{x=4} = 0 \quad (8)$$

$$-\sigma_{eff,i} \frac{\partial \phi_{s,i}}{\partial x} \Big|_{x=6} = i_{app} \quad (9)$$

where 1, 3, 4 and 6 are the boundary points in the direction of cell thickness (see Fig. 1),  $i_{app}$  is the current density applied to the battery electrode.

The charge conservation in the electrolyte solution is expressed as:

$$i_{e,i} = -k_{eff,i} \frac{\partial \phi_{e,i}}{\partial x} + \frac{2k_{eff,i}RT(1-t_+)}{F} \left( 1 + \frac{d \ln f_{\pm}}{d \ln c_i} \right) \frac{\partial \ln c_i}{\partial x} \quad (10)$$

where  $i = n, p$ . The effective electric conductivity of the electrolyte is defined by  $k_{eff,i} = k_{el,i}^{brug}$ . The boundary conditions are given by

$$\frac{\partial \phi_{e,i}}{\partial x} \Big|_{x=2} = \frac{\partial \phi_{e,i}}{\partial x} \Big|_{x=5} = 0 \quad (11)$$

where 2 and 5 are the boundary points in the cell thickness direction (see Fig. 1).

### 2.1.3. Energy conversion equations

The energy conversion equation in the lithium-ion battery is given by

$$\rho C_P \frac{\partial T}{\partial t} = \nabla \cdot \nabla (k_T T) + \dot{Q}_{ohm} + \dot{Q}_{act} + \dot{Q}_{rea} \quad (12)$$

The heat sources for the lithium-ion battery include the ohmic heat, the polarization heat and the reaction heat. They are calculated by

$$\begin{aligned} \dot{Q}_{ohm} = & \sigma_{eff,i} \left( \frac{\partial \phi_{s,i}}{\partial x} \right)^2 + k_{eff,i} \left( \frac{\partial \phi_{e,i}}{\partial x} \right)^2 + \frac{2k_{eff,i}RT(1-t_+)}{F} \left( 1 + \frac{d \ln f_{\pm}}{d \ln c_i} \right) \frac{\partial \ln c_i}{\partial x} \frac{\partial \phi_{e,i}}{\partial x} + a_i F j_i \Delta \phi_{SEI} \end{aligned} \quad (13)$$

$$\dot{Q}_{act} = a_i F j_i \eta_i \quad (14)$$

$$\dot{Q}_{rea} = a_i F j_i T \frac{dE_i}{dT} \quad (15)$$

where the first term on the right side of Eq. (13) is the ohmic heat due to electronic conductive resistance (i.e., the resistance of electrode materials and current collectors). The second and third terms are the ohmic heat due to ion conductive resistance (i.e., the  $\text{Li}^+$  transport resistance in electrolyte). The fourth term is the ohmic heat due to the solid electrolyte interface (SEI) film resistance.

The boundary condition for the energy balance is given by

$$q_0 = \epsilon (T_{amb}^4 - T^4) + h(T_{amb} - T) \quad (16)$$

where  $q_0$  is the heat flux on the battery surface.

### 2.1.4. Other equation

The electrochemical reaction rate on the surface of electrode particles is usually governed by the Butler–Volmer equation:

$$j_i = k_i \left( c_{s,max,i} - c_{s,surf,i} \right)^{\alpha_a} c_{s,surf,i}^{\alpha_c} c_i^{\alpha_a} \left\{ \exp \left( \frac{\alpha_a F \eta_i}{RT} \right) - \left[ \exp \left( - \frac{\alpha_c F \eta_i}{RT} \right) \right] \right\} \quad (17)$$

where  $i = n, p$ . The over-potential on the electrode particle surface is calculated by

$$\eta_i = (\phi_{s,i} - \phi_{e,i} - \Delta\phi_{SEI,i}) - E_i \quad (18)$$

where  $E$  is the open circuit potential of the electrode materials, which is dependent on the battery temperature and Li concentration at the particle surface.

## 2.2. Parallel-connected battery pack

In EV applications, the battery system consists of a number of single cells connected in serial or/and parallel to achieve the power and capacity requirements. Usually, the cylindrical battery stack is cooled by the air flowing along the axis [6,8] or the vertical axis direction [25]. The temperature of the cooling air increases along the air flowing direction, which induces the differences of the heat dissipation among the cells.

The discharge current and the output voltage for parallel-connected cells satisfy the Eqs. (18 and 19). It is known that the temperature distribution in the battery pack is not uniform. Therefore, the operating temperatures of cells are different each other. On the other hand, the internal resistance of the cell depends on the operating temperature. For parallel-connected cells, they operate at the same voltage, but different discharging currents due to different operating temperatures among them. This unbalanced discharging causes deviations of the discharging performances (e.g., voltage platform, discharging capacity, temperature rise and capacity degradation etc.) among the cells. This paper quantitatively investigates this type of the unbalanced discharging performances due to temperature differences between two parallel-connected cells.

$$I_{out} = I_1 + I_2 + \dots + I_n \quad (19)$$

$$V_{out} = V_{cell\ 1} = V_{cell\ 2} = \dots = V_{cell\ n} \quad (20)$$

## 2.3. Capacity fade of lithium-ion batteries

The capacity degradation of lithium-ion batteries is caused by several mechanisms associated with the unwanted side reactions. These reactions induce phase changes in the inserted electrode materials, active material dissolution, passive film formation, electrolyte decomposition and other negative effects [26]. Among these factors, the consumption of active lithium has been acknowledged as the main cause of the capacity degradation of lithium-ion batteries [18,20,27–30]. During charging/discharging cycle, the capacity degradation of lithium-ion batteries strongly depends on the temperature and can be estimated by a standard Arrhenius formula [2,18,20]. In this paper, the loss of active lithium in the battery is calculated by the expressions as Ref. [18]:

$$\frac{dc_{loss,N}(t)}{dt} = A_d \exp\left[\frac{-E_a}{RT(N,t)}\right] \quad (21)$$

$$c_{loss,N} = \int_0^{t_N} A_d \exp\left[\frac{-E_a}{RT(N,t)}\right] dt \quad (22)$$

where  $c_{loss,N}$  is the accumulated loss of active lithium in the discharging process of  $N$ th cycle,  $t_N$  is the total discharging time of  $N$ th cycle,  $T(N, t)$  is the time-dependent battery average temperature during  $N$ th discharging process,  $A_d$  and  $E_a$  represent the reference lithium loss and the activation energy. The Eqs. (21) and (22) have slight differences in the expressions presented by Ref. [18] where

the volume of electrode material is included in the parameter  $A_d$ . According to the Faraday's law, the accumulated capacity degradation after  $N$  charge/discharge cycles can be calculated by Ref. [31].

$$C_{loss\_total, N} = 26.8 \sum_{i=1}^N c_{loss,i} \quad (23)$$

where  $c_{loss,i}$  is the accumulated loss of active lithium in the discharging process of  $i$ th cycle.

## 3. Model parameters and experimental validation

### 3.1. Model parameters

The present work chooses a type of 26650 LiFePO<sub>4</sub> battery manufactured by Bak International (Tianjin) Limited, China, as the sample in the case study. The main technical parameters of the battery are listed in Table 1 and Table 2. The diffusivity  $D$ , the conductivity  $\kappa$  and the thermodynamic factor  $\upsilon$  for electrolyte are referred to Ref. [32]. The open circuit potentials of the electrode materials are from Refs. [33,34]. The density, heat capacity and thermal conductivity of the winding layer of the battery are referred to Refs. [35,36]. The electrochemical reaction rate and the coefficient of the Li diffusion in the electrode particles are assumed to follow the Arrhenius formula [4]. In this work, the coefficients of heat radiation and convection heat are estimated according to the changes in the battery temperature during discharging process, which are given to be  $0.85 \text{ Wm}^{-2} \text{ K}^{-1}$  and  $20 \text{ Wm}^{-2} \text{ K}^{-1}$ , respectively. From the references [2,18], the degradation rate of the battery capacity with cycle number remains approximately a constant value when the operating conditions are fixed. In this work, the cycling experiments on the battery were conducted with the constant current-constant voltage charging mode ( $3 \text{ C} \rightarrow 3.6 \text{ V} \rightarrow 0.02 \text{ C}$ ) and the constant current discharging mode ( $5 \text{ C} \rightarrow 2.0 \text{ V}$ ) at  $25^\circ \text{C}$  and  $40^\circ \text{C}$ , respectively. The experimental results show that the average capacity losses in each charging/discharging cycle are  $0.131 \text{ mAh}$  and  $0.243 \text{ mAh}$ , respectively. Then, the parameters  $A_d$  and  $E_a$  shown in the capacity degradation model are estimated to be  $0.01325 \text{ mol s}^{-1}$  and  $38200 \text{ J mol}^{-1}$ , respectively. The model simulations are performed using a finite-element software-COMSOL Multiphysics 4.2. The governing equations are discretized by the BDF (backward differentiation formulas) discretization method and solved by the direct linear solver MUMPS (Multifrontal Massively Parallel sparse direct Solver). Generally, the quadratic element orders are used for the discretization of control equations [39]. In this work, the quadratic element order is used for discretizing the control equations of the variables of  $\phi_e$ ,  $c$ , and  $T$ . For the electric potential ( $\phi_s$ ) equation, a linear element order is

**Table 1**  
Model parameters for the battery.

Parameters	Negative electrode	Separator	Positive electrode
$L_i$ (m)	$39 \times 10^{-6}$	$20 \times 10^{-6\text{m}}$	$55 \times 10^{-6\text{m}}$
$\sigma_i$ ( $\text{S m}^{-1}$ )	100 [37]		0.5 [37]
$\varepsilon_{s,i}$	0.585 <sup>m</sup>		0.513 <sup>m</sup>
$\varepsilon_{l,i}$	0.364 <sup>m</sup>	0.54 [37]	0.417 <sup>m</sup>
$r_{s,i}$ (m)	$6.5 \times 10^{-6\text{m}}$		$1.4 \times 10^{-6\text{m}}$
$c_{smax,i}$ ( $\text{mol m}^{-3}$ )	31370 [38]		22806 [38]
$c_{s0,i}/c_{smax,i}$	0.86 <sup>a</sup>		0.05 <sup>a</sup>
$c_{0,i}$ ( $\text{mol m}^{-3}$ )		1200 <sup>m</sup>	
$t_+$		0.363 [37]	
$\alpha_{a,i}/\alpha_{c,i}$	0.5		0.5
$brug,i$	2.4 <sup>a</sup>	1.5 <sup>a</sup>	1.8 <sup>a</sup>
$R_{SEI,i}$ ( $\Omega \text{ m}^2$ )	0.01 <sup>a</sup>		0

<sup>m</sup> Manufacturer; <sup>a</sup> Estimated by experiment data.

**Table 2**

Thermal property parameters for each materials of the battery.

Materials	$k_{Ti}$ (W m <sup>-1</sup> K <sup>-1</sup> )	$C_{pi}$ (J kg <sup>-1</sup> K <sup>-1</sup> )	$\rho_i$ (kg m <sup>-3</sup> )
Cu	401 [37]	3440 [37]	8900 [37]
Negative electrode	1.48 [37]	800 [37]	1400 <sup>m</sup>
Separator	1 [37]	1978 [35]	1200 [37]
Positive electrode	1.04 [37]	800 [37]	2100 <sup>m</sup>
Al	237 [37]	2420 [37]	2700 [37]
Electrolyte	0.6 [37]	2055 [35]	1130 [37]
Battery can	160 <sup>m</sup>	900 <sup>m</sup>	2700 <sup>m</sup>
Battery mandrel (Nylon)	0.26 <sup>a</sup>	1700 <sup>a</sup>	1150 <sup>m</sup>

<sup>m</sup> Manufacturer; <sup>a</sup> Estimated by experiment data.

employed as it can minimize the spurious oscillations [39]. The grid independency study is carried out on three different mesh sizes (See Table 3) with a time-step of 2 s. The simulation results show that the value differences between the simulated performance parameters (the discharging capacity, the discharging energy and the battery temperature rise) for different mesh size settings are negligible. In this work, the grid number of  $n_1 = 130$  and  $n_2 = 2957$  is used in the simulations. The time-step independency study is carried out with three different time-step setups (See Table 4). As shown in Table 4, there is little difference between different time-step settings. In this work, the time-step of 2 s is used in the simulations.

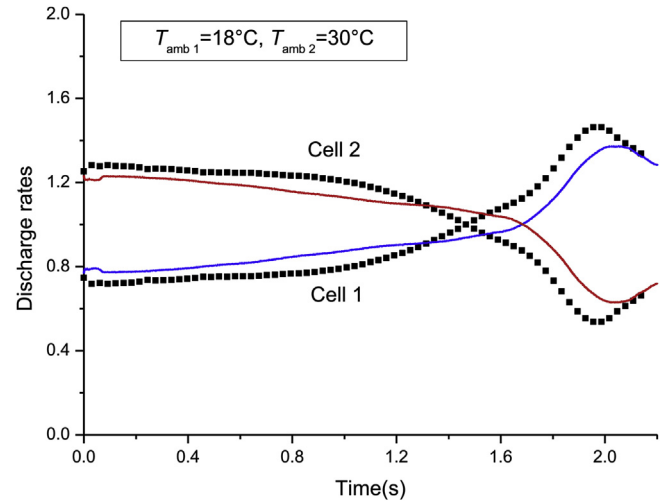
### 3.2. Experimental validation

The model validation experiments are conducted on a battery discharging/charging experiment platform. The experimental facilities include a constant temperature testing machine (BE-HL-150M8S, Bell Experiment Equipment Co., Ltd), a battery test system (BTS-5V20A, Shenzhen Neware Electronics Co., Ltd), a data acquisition system (Agilent 34970A, Agilent Technologies Inc.), a computer and a few thermal resistances. In the experiments, the constant temperature testing machine was used to precisely control the temperature environment during battery operations. The output voltage, current and temperature of the battery are measured during discharging process at different temperatures (5 °C, 15 °C and 25 °C). The temperature is measured by the thermal resistance at half-height position on the battery surface. Fig. 2 shows the output voltage and temperature rise from the experiments compared with the corresponding values from the simulations. The simulation results agree well with the experimental data. There are slightly larger deviations at the turning point of the voltage curve and at the beginning of the temperature curve. These errors are primarily from the estimation errors of diffusivity and conductivity for the electrolyte used in the model.

Fig. 3 shows the discharging currents from the experiments compared with that of simulations for two parallel-connected cells. In this case, the cells were discharged at different ambient temperatures. The Cell 1 and Cell 2 operate at 18 °C (the room temperature) and 30 °C (the temperature of the testing machine), respectively. The simulation results are consistent with the measured currents. The deviations between the simulations and the experiments are mainly caused by the estimation errors of

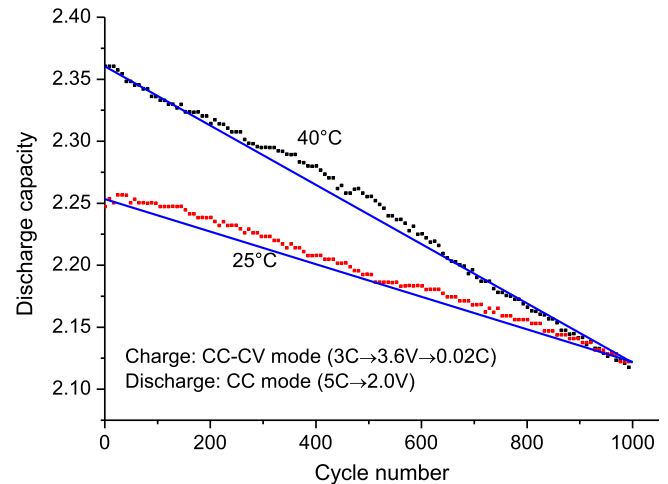
**Table 4**Overall the simulated discharge performance parameters with different time-steps (discharging with 2 C at 25 °C,  $n_1 = 130$  and  $n_2 = 2957$ ).

	$\Delta t = 1$ s	$\Delta t = 2$ s	$\Delta t = 4$ s
Battery temperature rise (°C)	7.36351	7.36351	7.36351
Discharging capacity (Ah)	2.20674	2.20087	2.18963
Discharging energy (Wh)	6.91590	6.89373	6.85856

**Fig. 3.** Comparison between the experimental (dots) and the simulated (solid lines) output voltage of two cells with parallel combination.

model parameters and the fluctuation of the room temperature.

Fig. 4 shows the comparison between the experimental and the simulated battery capacity degradation rates for cycling at 25 °C

**Fig. 4.** Comparison between the experimental (dots) and the simulated (solid lines) capacity degradation rates at different ambient temperatures.**Table 3**Overall the simulated discharge performance parameters on different grid number settings (discharging with 2 C at 25 °C,  $\Delta t = 2$  s).

	$n_1 = 65, n_2 = 1483$	$n_1 = 130, n_2 = 2957$	$n_1 = 259, n_2 = 5968$
Battery temperature rise (°C)	7.37538	7.37541	7.36351
Discharging capacity (Ah)	2.21042	2.20087	2.19504
Discharging energy (Wh)	6.92357	6.89373	6.87547

Note:  $n_1$  is the grid number of 1D electrochemical model and  $n_2$  is the grid number of 2D thermal model.



and 40 °C, respectively. It can be seen from Fig. 4 that the capacity degradation rate predicted by the proposed model is in accordance with the measured data.

#### 4. Results and discussions

As shown in Fig. 2(a), both the battery voltage platform and the discharging capacity lower as the ambient temperature decreases. The decrease of the discharging capacity at lower temperatures is mainly due to the decline of lithium diffusivity in the electrode materials. Both the lithium diffusivity of the electrode materials and the electrical conductivity of electrolyte decrease as the temperature decreases, which causes the drop of the voltage platform. The detailed analysis of temperature effects on the battery discharging performances can be found in our previous work [23]. As shown in Fig. 2(a), the battery performances are closely related to the operating temperature.

A battery pack with two parallel-connected 26650 LFP cells is studied in this work. Assuming the ambient temperature of Cell 1 is lower than that of Cell 2 by  $\Delta T$ . Fig. 5 shows the changes in the operating currents with time for the Cell 1 and Cell 2 during discharging with total current of 2 C. In these cases, the operating temperatures for Cell 1 are 5 °C (Fig. 5 (a) and (b)) and 10 °C (Fig. 5(c) and (d)), respectively. The temperature differences between Cell 1 and Cell 2 are given to be 5 °C (Fig. 5 (a) and (c)) and 10 °C (Fig. 5 (b) and (d)). The temperature differences cause the deviations of discharge current between the parallel-connected cells. In the early stage of discharging process, the cell at higher temperature experiences a larger current (see Fig. 5(a–d)). This can

be explained by the fact that the battery internal resistance decreases with temperature rising. As the discharging process is further carried out, the cell at higher temperature approaches to the fully discharged state sooner than that of the cell at lower temperature. Since the output voltages between the parallel-connected cells are equal, the current of the cell at higher temperature decreases significantly in order to offset the effect of its open circuit voltage. This causes the increase of the discharging current through the Cell 1 at lower temperature (see region B in Fig. 5). After the discharging process reaches approximately 90% DOD (depth of discharge) of the battery group, the capacity of the Cell 1 at lower temperature approaches to the full discharge state. The discharge current decreases for Cell 1 at lower temperature while it increases for the Cell 2 at higher temperature (see region C in Fig. 5).

It can be also seen from Fig. 5 that the differences in the discharging currents of parallel-connected cells decrease gradually with time in the region A, particularly in the cases of larger temperature differences or higher ambient temperatures. This is mainly due to that the cell internal resistance is highly dependent on the operating temperature. During discharging process, the battery output voltage can be evaluated by

$$V_{\text{out}} = V_{\text{OCV}} - I \cdot R_{\text{int}} \quad (24)$$

where  $V_{\text{out}}$  and  $V_{\text{OCV}}$  are the output voltage and the open circuit voltage of the lithium-ion battery, respectively.  $I$  is the operating current during discharging process.  $R_{\text{int}}$  is the battery internal resistance. According to Eq. (19) for the voltage equation of parallel-connected battery group, the following equation can be obtained.

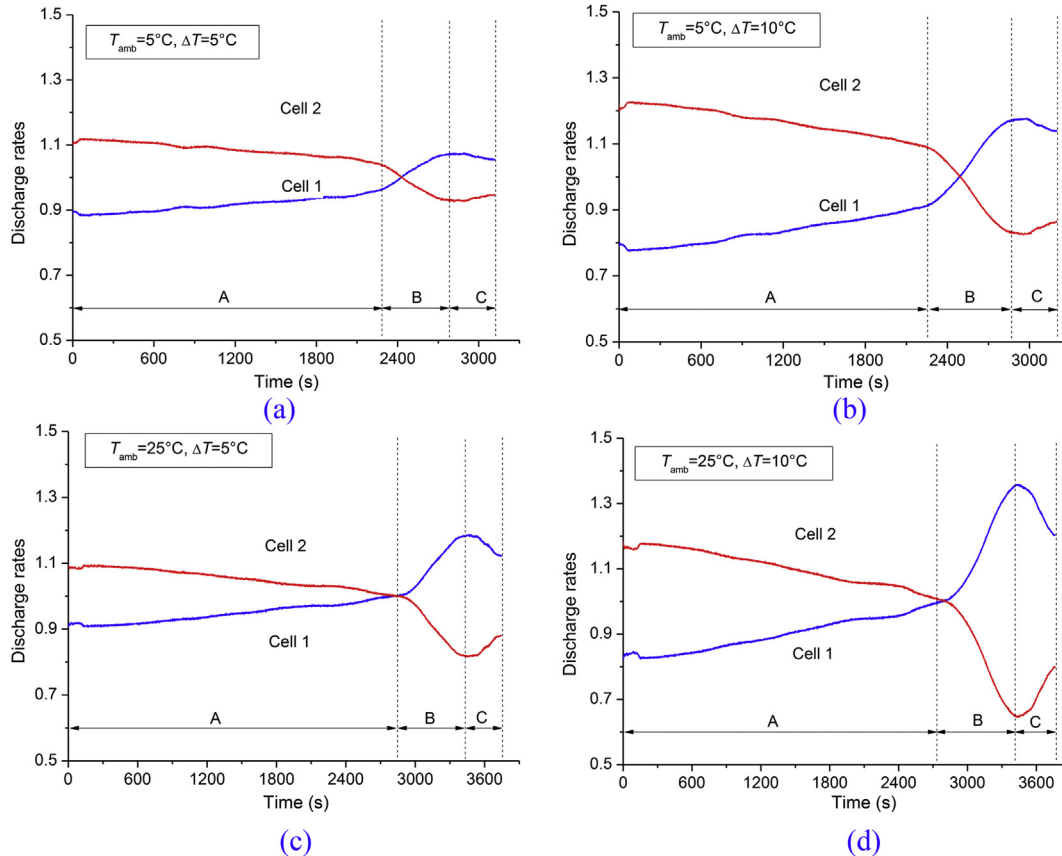


Fig. 5. Current curves of two parallel connected batteries during discharging with total current of 2 C at different temperature setups: (a)  $T_{\text{amb}} = 5^\circ\text{C}$ ,  $\Delta T = 5^\circ\text{C}$ ; (b)  $T_{\text{amb}} = 5^\circ\text{C}$ ,  $\Delta T = 10^\circ\text{C}$ ; (c)  $T_{\text{amb}} = 25^\circ\text{C}$ ,  $\Delta T = 5^\circ\text{C}$ ; (d)  $T_{\text{amb}} = 25^\circ\text{C}$ ,  $\Delta T = 10^\circ\text{C}$ .

$$V_{OCV_{TH}} - I_{TH} \cdot R_{int_{TH}} = V_{OCV_{TL}} - I_{TL} \cdot R_{int_{TL}} \quad (25)$$

For discharging process of the parallel-connected battery pack, the open circuit voltage of the cell at higher temperature is lower than that of the cell at lower temperature because it is discharged under larger current and its capacity goes down faster (See Fig. 5). That means  $V_{OCV_{TH}} < V_{OCV_{TL}}$ . Then,

$$\frac{I_{TH}}{I_{TL}} < \frac{R_{int_{TL}}}{R_{int_{TH}}} \quad (26)$$

Generally, the internal resistance of the lithium-ion battery is the function of temperature, DOD and operating current [40]. The battery internal resistance equals the sum of the ohmic resistance and polarization resistance, which are calculated by HPPC (hybrid pulse power characterization) method [40,41]. Fig. 6 shows the change curves of the ratios of  $I_{TH}/I_{TL}$  and  $R_{int_{TL}}/R_{int_{TH}}$  during discharging process of the parallel-connected battery pack under the operating conditions of  $T_{amb} = 25^\circ\text{C}$  and  $\Delta T = 10^\circ\text{C}$ . As shown in Fig. 6, the minimum of  $I_{TH}/I_{TL}$  is 0.48, which is lower than that of  $R_{int_{TL}}/R_{int_{TH}}$  (i.e., 0.83). This is well in accordance with the Eq. (25). With the proceeding of the discharging process, the internal resistance of the cell at lower temperature decreases faster than that of the cell at higher temperature, particularly in the cases of larger temperature differences or higher ambient temperatures. This induces the ratio of the discharging current between the cells is gradually close to 1 (See region A in Fig. 5). Similarly, the difference between the cell internal resistances also increases with increasing of the temperature difference, which enlarges the differences of the discharge current between the parallel-connected cells (See regions A and C in Fig. 5).

Fig. 7(a) and Fig. 7(b) show the voltage curves and the discharging capacities of the battery pack with parallel combination at different ambient temperature setups. As the temperature differences between the parallel-connected cells increases, both the output voltage and the discharging capacity of the battery pack increase slightly. These increments are enlarged in the case of lower ambient temperatures. Similarly, this is explained by the dependence of the cell internal resistance on the temperature. Although, the larger temperature differences induce the more difference of the internal resistance between cells, the total internal resistance of the battery pack changes little. According to the calculations, the total internal resistance at the temperature difference of  $10^\circ\text{C}$  is

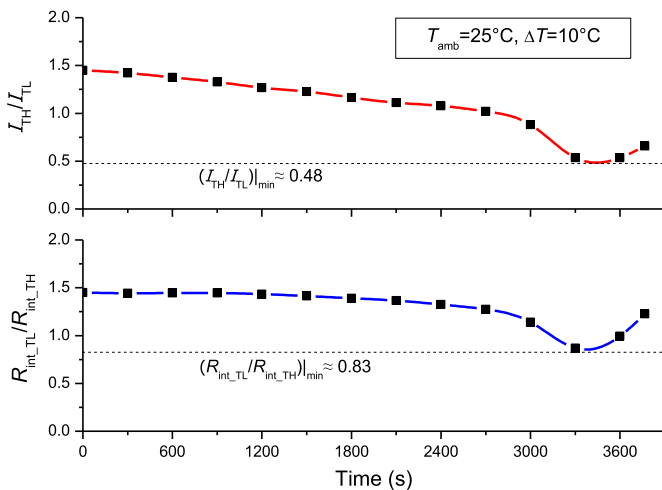


Fig. 6. The changes of  $I_{TH}/I_{TL}$  and  $R_{int_{TL}}/R_{int_{TH}}$  during discharging process of the parallel-connected cells at  $T_{amb} = 25^\circ\text{C}$  and  $\Delta T = 10^\circ\text{C}$ .

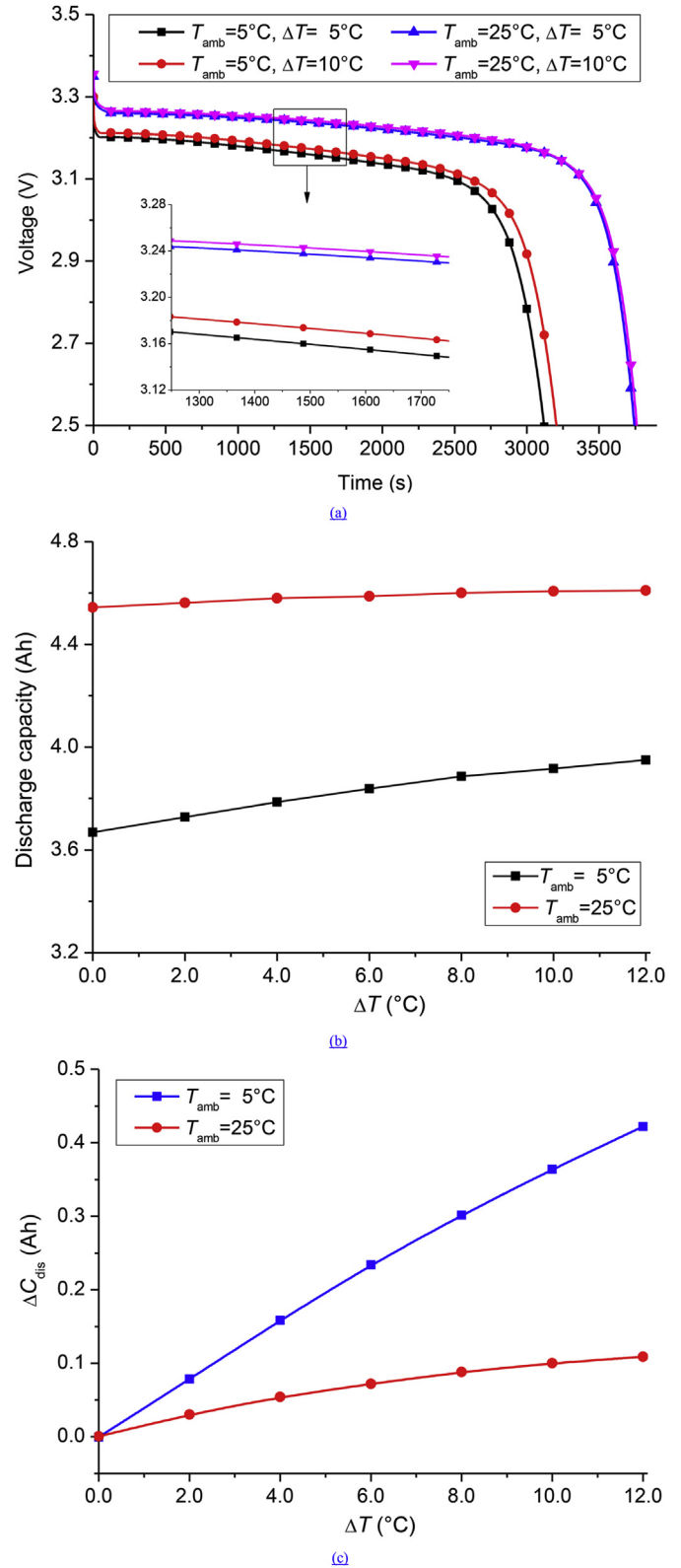


Fig. 7. Discharging performances of the battery pack with parallel combination at different temperature setups: (a) Discharging voltage curves of the battery pack; (b) Discharging capacities of the battery pack; (c) Differences between the discharging capacities of two cells.

approximately 10% lower than that of  $5^\circ\text{C}$ .

Fig. 7(c) shows the differences between the discharging capacities of the parallel-connected cells at different ambient

temperatures setups (where  $\Delta C_{dis} = C_{dis\_TH} - C_{dis\_TL}$ ). As shown in Fig. 7(c), the capacity differences between the cells increase with the temperature difference increasing, especially in the case of lower ambient temperatures. This induces the imbalance discharge phenomenon between the cells in the parallel combination, which potentially reduces the battery pack performances, such as the capacity degradation and the overcurrent discharge. Fig. 8 shows the average capacity loss per cycle for the battery pack with parallel combination at different ambient temperature setups. It can be seen from Fig. 8 that the capacity loss rate increases with increasing the temperature difference between the parallel-connected cells. This trend is magnified as the ambient temperature increases. Therefore, the temperature differences among cells in the battery pack must be well controlled ( $\leq 5^\circ\text{C}$ ), which can minimize the unbalanced discharging and aging among the cells and maximize the serve life and discharging performances for the battery pack.

## 5. Conclusions

This paper presents a study of the temperature unbalanced discharging and aging on the parallel-connected cells for lithium-ion batteries. A thermal–electrochemical model is developed to simulate the discharging process for the parallel-connected cells. The influences of the temperature differences among the cells on the discharging and aging performances are investigated by simulations and experiments. For the parallel-connected cells, the cell at higher temperature experiences larger current in the early stage of the discharging process (before around 75% DOD). As the discharging process gradually approaches the turn point of the output voltage of the battery pack, the discharging current decreases greatly for the cell at higher temperature while it goes up for the cell at lower temperature. After the discharging process reaches approximately 90% DOD, the current through the cell at higher temperature rises again and the current through the cell at lower temperature goes down. The effect of temperatures difference among the parallel-connected cells on the overall output voltage and discharge capacity is negligible for the battery pack. However, it significantly aggravates the unbalanced discharging phenomenon between the cells.

A simplified capacity loss model was proposed for the lithium-ion batteries and was used to assess the capacity degradation performances for the parallel-connected cells. For the battery pack with parallel combination, the capacity loss rate increases as the

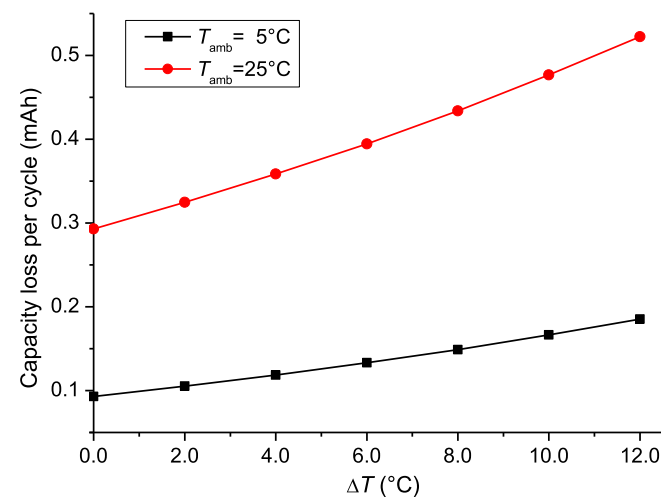


Fig. 8. Capacity loss rate of the battery pack with parallel combination at different ambient temperature setups.

temperature difference between the cells increases. The higher is the operating temperature of cell, the higher is the capacity loss rate of the battery pack. The temperature difference among cells in the battery pack has to be well controlled to minimize the losses of the discharge capacity and maximize the serve life of the battery pack.

## Acknowledgment

This work was funded by the Industrial Research Foundation of Shaanxi Province (Grant No. 2014K06-27).

## Nomenclature

$a_i$	specific surface area, $\text{m}^{-1}$
$brug$	Bruggeman tortuosity exponent
$c$	electrolyte concentration in the solution phase, $\text{mol m}^{-3}$
$C_{loss}$	loss of active lithium during the charging/discharging process, mol
$C_p$	heat capacity, $\text{J kg}^{-1} \text{K}^{-1}$
$C_s$	Li concentration in electrode particles, $\text{mol m}^{-3}$
$C_{s\_max}$	theoretical maximum Li concentration in electrode particles, $\text{mol m}^{-3}$
$C_{s\_surf}$	Li concentration on the surface of electrode particles, $\text{mol m}^{-3}$
$D$	diffusion coefficient of electrolyte, $\text{m}^2 \text{s}^{-1}$
$D_s$	diffusion coefficient of Li in electrode particles, $\text{m}^2 \text{s}^{-1}$
$E$	open circuit voltage of electrodes, V
$F$	Faraday's constant, $\text{C mol}^{-1}$
$f_{\pm}$	mean molar activity coefficient of an electrolyte
$i_{app}$	the current density applied to the battery electrode, $\text{A m}^{-2}$
$i_e$	solution phase current density, $\text{A m}^{-2}$
$i_s$	solid phase current density, $\text{A m}^{-2}$
$j_i$	surface reaction rate, $\text{mol m}^{-2} \text{s}^{-1}$
$k$	reaction rate constant at reference temperature, $\text{m}^{2.5} \text{mol}^{-0.5} \text{s}^{-1}$
$k_{T,i}$	thermal conductivity, $\text{W m}^{-1} \text{K}^{-1}$
$L_i$	electrode thickness, m
$\dot{Q}_{act}$	active polarization heat generation rate, $\text{W m}^{-3}$
$\dot{Q}_{ohm}$	ohmic heat generation rate, $\text{W m}^{-3}$
$\dot{Q}_{rea}$	reaction heat generation rate, $\text{W m}^{-3}$
$R$	gas constant, $\text{mol k}^{-1}$
$r$	coordinate along radius direction of the electrode particles, m
$r_s$	radius of electrode particle, m
$R_{in}$	the battery internal resistance, $\Omega$
$R_{SEI}$	resistance of the film at solid electrolyte interphase, $\Omega \text{m}^2$
$T$	temperature, K
$t_+$	transference number of Li ions species dissolved in liquid
$V_{OCV}$	the open circuit voltage of the battery, V
$V_{out}$	the output voltage of the battery, V
$x$	coordinate along the thickness direction of cell components, m

## Greek letters

$\alpha_a$	transfer efficient for anodic current
$\alpha_c$	transfer efficient for cathodic current
$\varepsilon_s$	volume fraction of active material
$\varepsilon_l$	volume fraction of electrolyte
$\kappa$	ionic conductivity of electrolyte, $\text{S m}^{-1}$
$\rho$	Density, $\text{kg m}^{-3}$
$\sigma$	electronic conductivity of solid matrix, $\text{S m}^{-1}$
$\eta$	activation over potential of an electrode reaction, V



$\varphi_s$	solid phase voltage, V
$\varphi_e$	solution phase voltage, V
$\Delta\varphi_{SEI,i}$	voltage drop result from the SEI film resistance, V

### Subscripts

N	negative
p	positive
s	separator
TH	higher temperature cell
TL	Lower temperature cell
0	initial state of discharge

### References

- [1] K.E. Aifantis, S.A. Hackney, R.V. Kumar, *High Energy Density Lithium Batteries: Materials, Engineering, Applications*, John Wiley & Sons, 2010.
- [2] J. Wang, P. Liu, J. Hicks-Garner, E. Sherman, S. Soukiazian, M. Verbrugge, H. Tatara, J. Musser, P. Finamore, *J. Power Sources* 196 (2011) 3942–3948.
- [3] M.B. Pinson, M.Z. Bazant, *J. Electrochem. Soc.* 160 (2013) A243–A250.
- [4] N. Yang, X. Zhang, G. Li, *Electrochim. Acta* 151 (2015) 63–71.
- [5] N. Yang, X. Zhang, G. Li, D. Hua, *Appl. Therm. Eng.* 80 (2015) 55–65.
- [6] R. Sabbah, R. Kizilel, J. Selman, S. Al-Hallaj, *J. Power Sources* 182 (2008) 630–638.
- [7] R. Mahamud, C. Park, *J. Power Sources* 196 (2011) 5685–5696.
- [8] J. Xun, R. Liu, K. Jiao, *J. Power Sources* 233 (2013) 47–61.
- [9] X. Xu, R. He, *Renew. Sustain. Energy Rev.* 29 (2014) 301–315.
- [10] L. Fan, J. Khodadadi, A. Pesaran, *J. Power Sources* 238 (2013) 301–312.
- [11] H. Teng, K. Yeow, in: *SAE Technical Paper*, 2012.
- [12] K. Yeow, H. Teng, M. Thelliez, E. Tan, in: *SAE Technical Paper*, 2012.
- [13] X. Zhang, X. Kong, G. Li, J. Li, *Energy* 64 (2014) 1092–1101.
- [14] Z. Rao, S. Wang, *Renew. Sustain. Energy Rev.* 15 (2011) 4554–4571.
- [15] P. Ramadass, B. Haran, R. White, B.N. Popov, *J. Power Sources* 112 (2002) 606–613.
- [16] P. Ramadass, B. Haran, R. White, B.N. Popov, *J. Power Sources* 112 (2002) 614–620.
- [17] P. Ramadass, B. Haran, R. White, B.N. Popov, *J. Power Sources* 123 (2003) 230–240.
- [18] C. Kuan-Cheng, L. Chi-Hao, Y. Sheng-Fa, L. Yu-Han, H. Chih-Sheng, C. Kuo-Ching, *J. Power Sources* 263 (2014) 75–84.
- [19] M.-S. Wu, C.-Y. Lin, Y.-Y. Wang, C.-C. Wan, C. Yang, *Electrochim. Acta* 52 (2006) 1349–1357.
- [20] R. Gogoana, M.B. Pinson, M.Z. Bazant, S.E. Sarma, *J. Power Sources* 252 (2014) 8–13.
- [21] M. Doyle, T.F. Fuller, J. Newman, *J. Electrochem. Soc.* 140 (1993) 1526–1533.
- [22] M. Doyle, J. Newman, A.S. Gozdz, C.N. Schmutz, J.M. Tarascon, *J. Electrochem. Soc.* 143 (1996) 1890–1903.
- [23] N. Yang, X. Zhang, G. Li, *J. Power Sources* 272 (2014) 68–78.
- [24] D. Bernardi, E. Pawlikowski, J. Newman, *J. Electrochem. Soc.* 132 (1985) 5–12.
- [25] X. Li, F. He, L. Ma, *J. Power Sources* 238 (2013) 395–402.
- [26] P. Arora, R.E. White, M. Doyle, *J. Electrochem. Soc.* 145 (1998) 3647–3667.
- [27] M. Dubarry, B.Y. Liaw, *J. Power Sources* 194 (2009) 541–549.
- [28] J. Vazquez-Arenas, M. Fowler, M. Xiaofeng, S. Chen, *J. Power Sources* 215 (2012) 28–35.
- [29] P. Ramadass, B. Haran, P.M. Gomadam, R. White, B.N. Popov, *J. Electrochem. Soc.* 151 (2004) A196–A203.
- [30] G. Ning, R.E. White, B.N. Popov, *Electrochim. Acta* 51 (2006) 2012–2022.
- [31] S. Venkatraman, V. Subramanian, S. Gopu Kumar, N. Renganathan, N. Muniyandi, *Electrochem. Commun.* 2 (2000) 18–22.
- [32] L.O. Valøen, J.N. Reimers, *J. Electrochem. Soc.* 152 (2005) A882–A891.
- [33] M. Guo, G. Sikha, R.E. White, *J. Electrochem. Soc.* 158 (2011) A122–A132.
- [34] R.E. Gerver, J.P. Meyers, *J. Electrochem. Soc.* 158 (2011) A835–A843.
- [35] L. Saw, Y. Ye, A. Tay, *Energy Convers. Manag.* 75 (2013) 162–174.
- [36] S.C. Chen, Y.Y. Wang, C.C. Wan, *J. Electrochem. Soc.* 153 (4) (2006) A637–A648.
- [37] Y. Ye, Y. Shi, A.A.O. Tay, *J. Power Sources* 217 (2012) 509–518.
- [38] M. Safari, C. Delacourt, *J. Electrochem. Soc.* 158 (2011) A562–A571.
- [39] COMSOL AB, *COMSOL Multiphysics User's Guide*. Version: COMSOL Multiphysics 4.3, May, 2012.
- [40] T.T. Lou, W.G. Zhang, H.Y. Guo, J.S. Wang, in: *Advanced Materials Research*, Trans Tech Publ, 2012, pp. 246–251.
- [41] J.R. Belt, in, *Idaho National Laboratory*, 2010.